

ARTICLE

<https://doi.org/10.1038/s42003-019-0422-6>

OPEN

Motor torque measurement of *Halobacterium salinarum* archaeellar suggests a general model for ATP-driven rotary motors

Seiji Iwata¹, Yoshiaki Kinoshita ¹, Nariya Uchida², Daisuke Nakane ¹ & Takayuki Nishizaka¹

It is unknown how the archaellum—the rotary propeller used by Archaea for motility—works. To further understand the molecular mechanism by which the hexameric ATPase motor protein Flal drives rotation of the membrane-embedded archaellar motor, we determined motor torque by imposition of various loads on *Halobacterium salinarum* archaella. Markers of different sizes were attached to single archaella, and their trajectories were quantified using three-dimensional tracking and high-speed recording. We show that rotation slows as the viscous drag of markers increases, but torque remains constant at 160 pN·nm independent of rotation speed. Notably, the estimated work done in a single rotation is twice the expected energy that would come from hydrolysis of six ATP molecules in the hexamer, indicating that more ATP molecules are required for one rotation of archaellum. To reconcile the apparent contradiction, we suggest a new and general model for the mechanism of ATP-driven rotary motors.

¹Department of Physics, Gakushuin University, 1-5-1 Mejiro, Toshima-ku, Tokyo 171-8588, Japan. ²Department of Physics, Tohoku University, Sendai 980-8578, Japan. Correspondence and requests for materials should be addressed to D.N. (email: daisuke.nakane@gakushuin.ac.jp) or to T.N. (email: takayuki.nishizaka@gakushuin.ac.jp)

Motile archaea swim using surface appendages called archaella (previously named “archaeal flagella”), which are thrust-generating rotating helical filaments analogous to bacterial flagella¹. Although the bacterial flagellum consists of >30 different proteins, the archaellum is built from as few as 7 proteins, none of which are homologous to flagellar proteins². Instead, the archaellum is evolutionarily related to bacterial type IV pili. Recent structural and functional studies of protein components have begun to provide us a model of archaellar architecture^{1,3–5}. The mechanism of archaellar rotation, however, remains unclear, in part due to the lack of biophysical measurements that would constrain mechanistic models.

Components of the archaellar motor have been identified and biochemically characterized, providing the first steps to understand the mechanism of rotation³. Crucially, the archaellum is driven by ATP hydrolysis⁶ instead of proton flux as in the bacterial motor. The core archaellar motor is composed of the transmembrane protein FlaJ, ATPase FlaI, and associated FlaH. FlaI forms a hexamer^{7,8} that likely drives rotation, although it is unclear how FlaI generates torque. It is also unclear whether FlaI is static relative to the cell body or whether it rotates relative to the cell body together with the archaellum. FlaI has been shown to hydrolyze ATP⁸, and although the associated FlaH has an ATP binding motif⁹, there is no evidence that FlaH hydrolyzes ATP. Furthermore, no other archaellar components have been implicated as energy-transducing proteins, indicating that FlaI powers archaellar rotation alone, with a catalytic cycle involving sequential hydrolysis of six ATP molecules. Despite these biochemical insights, however, little is known of the physics of archaellar rotation.

We previously characterized archaellar function in the model organism *Halobacterium salinarum* using advanced fluorescent microscopy¹⁰. Challenges manipulating motor load, however, prevented us from measuring torque. To gain insights into the molecular mechanism underlying how FlaI drives rotation, we developed methods to measure archaellar motor torque. We found that archaellar torque remains constant at 160 pN·nm independent of rotation speeds between 0.5 and 30 Hz. Unexpectedly, the estimated work done in a single rotation was higher than the expected energy input that would come from the hexameric FlaI architecture, suggesting a model for the mechanism of archaellar motor rotation involving hydrolysis of more than one ATP molecule per FlaI subunit per full rotation.

Results

3D rotation assay with beads. Toward measuring archaellar motor torque, we developed protocols to attach markers to add viscous friction to rotating archaella. We previously described methods to immobilize cells on a glass surface to visualize rotation of archaella using fluorescent labeling¹⁰. Here we developed methods to attach fluorescent beads to *H. salinarum* archaella and visualized their rotation using a high-speed complementary metal oxide semiconductor (CMOS) camera (Fig. 1a). Beads rotated continuously (Fig. 1b and Supplementary Movie 1) both clockwise (CW) and counter-clockwise (CCW). As expected from previous results showing that archaella protrude obliquely from the cell¹⁰, trajectories of beads were ellipsoidal in the *xy*-plane (cf., Fig. 1e, upper panel). To check whether the bead orbit was the projection of a true circle and, if so, to estimate its radius, we applied three-dimensional (3D) tracking^{11,12} to the bead assay. A wedge prism at the equivalent back focal plane of the objective lens divided the image (Fig. 1c), enabling us to reconstruct the bead’s 3D trajectory from the change in relative displacement between the center positions of the two images, as previously described¹¹ (Fig. 1d). We identified the plane on which the orbit

became circular by a rotational search of the two angles in the polar coordinate (Fig. 1e; upper and lower panels are reconstructions of the same dataset viewed from different directions), enabling us to plot the rotation of each archaellum in its true plane of rotation (Fig. 1f). This measurement enabled quantification of archaellar rotation speed in both directions: 21.8 and 21.5 Hz for CW and CCW rotation, respectively, when using 210-nm-diameter beads as markers (Fig. 1g).

Archaella rotation rate depends on load. To determine archaellar rotation speeds under varying loads, we varied the sizes of the attached beads. Rotation rate decreased as we increased bead diameter (Fig. 2a) to a limit of 1 μm ; larger beads did not rotate smoothly, perhaps due to intermittent collisions with the glass surface. To impose higher viscous loads, we therefore used the tethered-cell assay¹⁰ (see Fig. 2b). Two patterns of rotation were observed: smooth rotation without pauses as exemplified in Fig. 2a, b and Supplementary Fig. 1A; and saw-tooth rotation with unitary steps as previously observed¹⁰ and shown in Supplementary Fig. 1B. Reasoning that pauses relating to the slow rate-limiting chemical step(s) inhibit torque estimation (as with the difference between “rotation rate” and “stepping rate” in the F_1 -ATPase rotary motor^{13,14}), we selected only cases with smooth rotation for further analysis. Rotation rate varied depending on marker diameter (Fig. 2d), decreasing as size increased (Fig. 2e), indicating that the archaellar motor in *H. salinarum* has an upper limit to its rotation rate of ~ 25 Hz, as an extrapolation in Fig. 2e, which was reduced by the viscous drag of the attached beads. Additional loads further reduced rotation rates to ~ 1 Hz while maintaining smooth unidirectional rotation. This observation is similar to the other, although unrelated, ATP-driven rotary motor, the F_1 -ATPase, which exhibits smooth rotation even when rotation rate slows to 1% the unloaded speed¹⁴.

Estimation of torque. It was unclear whether archaellar torque was constant under different loads. To calculate archaellar torque, therefore, we plotted rotation rate as a function of the viscous friction of attached markers. In conventional analyses of the bacterial flagellar motor, torque is plotted against speed in a linear scale^{15–17}, based on the assumption that the viscous friction of single flagellum against the surrounding media can be calculated. Here, however, we assumed that we could not directly estimate torque in individual trajectories because archaellum lengths are unknown in each measurement, and eccentric archaellar filament rotation contributes non-negligible additional drag. We thus plotted rotation rate against the viscous friction of markers (Fig. 3). Rotation rate was directly determined from our measurements; to estimate viscous friction in each trajectory, we estimated the viscosity of the solution, η , to be 1.35×10^{-3} Pa·s using a viscometer and used this to calculate viscous friction from the shape and size of markers and their radius of rotation (see “Methods” section).

Using these results, we estimated archaellar motor torque. If the motor produces constant torque T_a in any condition regardless of viscous drag, the rotation rate, f , will be inversely proportional to the viscous friction, γ , as $f = T_a/2\pi\gamma$. Our data confirmed this relationship under high loads, but indicated an additional friction factor, γ_a , that contributed apparent additional drag that becomes dominant at fast rotation under low loads. This parameter therefore represents a frictional drag factor in addition to that of the attached bead. Incorporating γ_a , we found that $f = T_a/2\pi(\gamma + \gamma_a)$, with $T_a = 120$ pN·nm and $\gamma_a = 0.60$ pN·nm·s for our dataset (indicated by the dotted line in Fig. 3).

We refined T_a and γ_a values by correcting for the interaction of the bead with the glass surface, as the surface suppresses flow

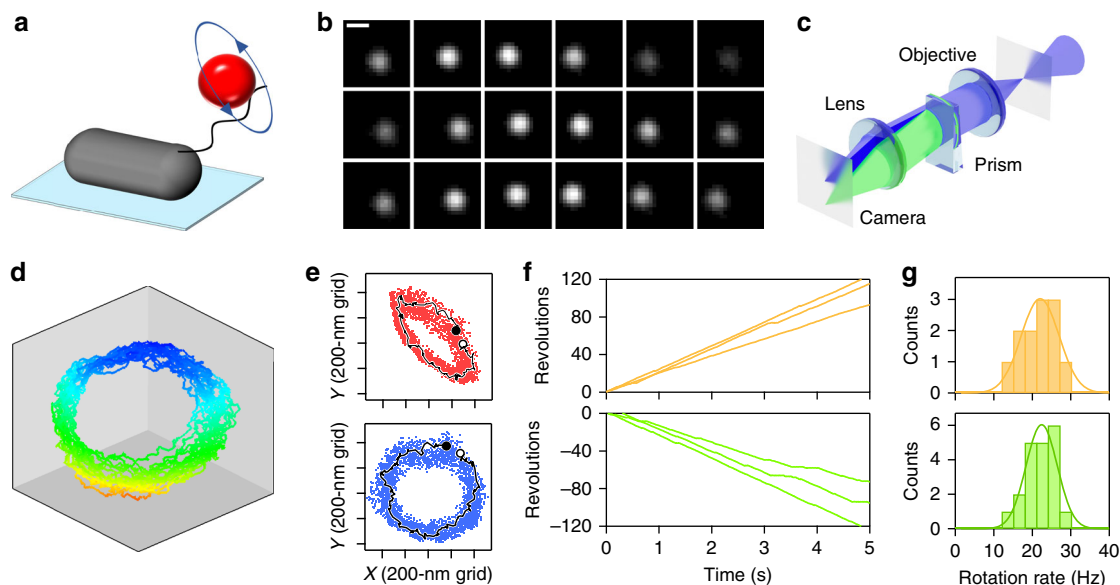


Fig. 1 Rotation of a fluorescent polystyrene bead attached to an archaeum of a cell immobilized to a glass surface. **a** Schematic of the experimental set-up. **b** Sequential micrographs of a rotating 490-nm-diameter bead captured in 10 ms intervals. Scale bar, 0.5 μm . **c** Schematic illustration of our optical path set-up between the equivalent sample plane (eSP) of the optical microscope and CCD camera to track three-dimensional (3D) motion of a bead as point light source. Half of the blue light is diffracted by a wedge prism, which is located at the equivalent back focal plane of the objective, and so two separate images are focused on the camera plate. **d** 3D plot of location of the bead bound to an archaeum over time. Different colors represent height from the glass surface. **e** xy-trajectory of bead position (dots) and representative one rotation (thin black line; starting from the open circle and ending at the closed circle). Upper, raw data. Lower, same dataset reoriented in 3D so that the circular rotation is coincident with the xy-plane of the plot. **f** Examples of time course of rotation in clockwise (CW; upper) and counter-clockwise (CCW; lower) directions. **g** Histograms of rotational rate for CW (upper) and CCW (lower). In **d-g**, 210-nm-diameter beads were used as markers

induced by the moving bead, leading to increased frictional drag. We corrected for this effect using correction factors estimated based on hydrodynamic calculation¹⁸, resulting in a shift of data points to the right (see black line in Fig. 3; see “Methods” section for the factors). This correction enabled us to refine our motor torque calculation to be 160 pN-nm. Similarly, we re-estimated γ_a , the additional viscous friction parameter, to be $\gamma_a = 0.81$ pN-nm-s. The formulation based on both T_a and γ_a is applicable as shown in the apparent torque plot against rotation rate (Supplementary Fig. 2A, B). Constant torque was shown after subtraction of the contribution of γ_a (Supplementary Fig. 2C) in the range of our measurements, which contrasted with the torque/speed behavior of the bacterial flagellar motor in which torque declines at lower loads (see Fig. 5 in ref. ¹⁵ and Fig. 4 in ref. ¹⁷).

Discussion

We have described method development to measure the torque of the *H. salinarum* archaeellar motor. We found that the motor’s torque output was 160 pN-nm regardless of rotation rate, in contrast to the bacterial flagellar motor in which torque is reduced for lower loads. Strikingly, as discussed below, this torque is approximately twice the anticipated torque that hydrolysis of six ATP molecules per full rotation could generate. We also identified an additional viscous friction factor, γ_a .

What is the physical basis for the additional γ_a factor? We speculated two models: in Model A, γ_a represents the frictional drag coefficient of the archaeum itself, as seen with the viscous drag measured for bacterial flagella;^{15–17} in Model B, γ_a is due to the mechanochemical chemical cycle, independent of load. To assess Model A, we calculated the drag coefficient of an archaeum, approximating it as a helical screw of appropriate dimensions¹⁰. We calculated an estimated archaeellar drag coefficient of 0.7 pN-nm-s (see “Methods” section), consistent with our γ_a value of 0.81 pN-nm-s. We also confirmed the length of archaeella on

cells prepared for our flow chamber using electron microscopy (Supplementary Fig. 3). Archaeellar filaments averaged 2.6- μm long immediately after shearing, re-growing to 4.6 μm after 2 h. The parameter used in the above is within this range. Model B, in which rotation rate with a constant torque has a rate-limiting step, $f(\gamma) = (1/f_{\text{no load}} + 2\pi\gamma/T_a)^{-1}$ (see Fig. 2 in ref. ¹⁴), is also consistent with our observations. Key chemical step(s), such as hydrolysis of ATP or ATP binding, are the rate-limiting steps, resulting in $f_{\text{no load}}$ as an upper limit for rotation. Also, the above equation turns to the same formulation in the legend of Fig. 3 with the assignment of $\gamma_a = T_a/2\pi f_{\text{no load}}$, and so discrimination between Models A and B is not possible in the fitting curve in Fig. 3. To assess Model B, it may be necessary to construct a ghost model of archaea analogous to that of the ATP-driven gliding machinery in *Mycoplasma mobile* (refs. ^{19,20}; the ghost model enabled us to change the concentration of ATP), although we anticipate that this may be technically challenging.

Our results show that the archaeellar motor produces constant torque independent of load, an observation that hints at the underlying molecular mechanism. Constant torque is also seen in the F_1 -ATPase (ref. ¹³), the soluble subcomplex of F_0F_1 ATP synthase but not the bacterial flagellar motor or linear motors driven by ATP hydrolysis, such as myosin, in which the force per motor is concave in relationship to load²¹, or kinesin, which linearly changes speed with load^{22,23}. In the case of the bacterial flagella motor, torque is constant up to a certain speed, after which it drops to zero, behavior believed to be a hallmark of the torque generation mechanism^{15,17}. Although FlaI and the α/β -subunits of the F_1 -ATPase (which include the catalytic site) are not closely related, their common architecture containing multiple symmetrically arranged catalytic sites in a cylinder evidently results in a common rotary mechanism.

Unexpectedly, however, our result indicates that motor torque exceeds that anticipated by hydrolysis of six ATP molecules per

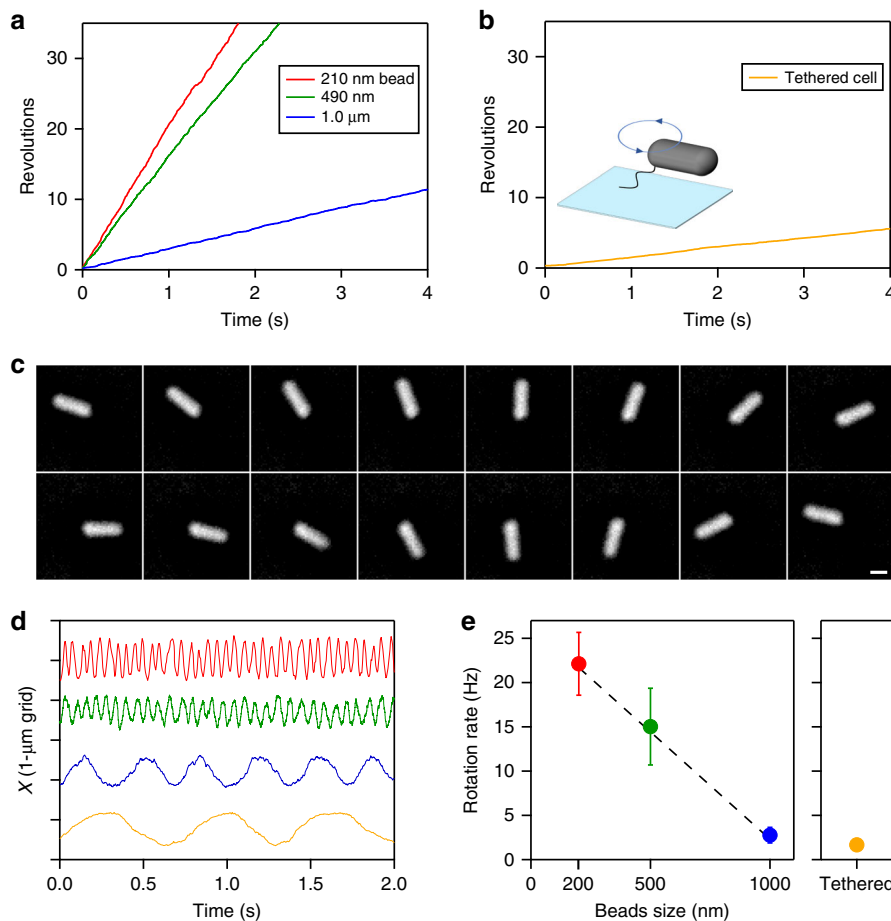


Fig. 2 Archaeella rotation rate is inversely proportional to load. **a** Example time courses of rotation of beads of different size. In all figures, red, green, blue, and yellow colors represent 210-nm, 490-nm, 1.0- μm diameter bead, and tethered cell, respectively. **b** An example time course of cell rotation in a tethered-cell assay. **c** Sequential phase-contrast micrographs of a tethered cell at 72 ms intervals. Image contrasts have been inverted for clarity. Scale bar, 1 μm . **d** Time courses of displacements of the center of markers. **e** Rotation rates of markers of different sizes. Error bars show standard deviations. The sources of data points are shown as values along the axis of ordinate in Fig. 3. Dotted line shows a linear fit, $V = A/\phi + B$, where V is rotation rate; ϕ diameter of bead; $B = 27$ Hz, an intercept; and $A = -0.024$ Hz nm $^{-1}$, a proportional coefficient

rotation—i.e., resulting from one ATP hydrolyzed per FlaI subunit. Our estimated torque of 160 pN·nm (Fig. 3) requires work for a single rotation to be $2\pi T_a \sim 1000$ pN·nm. This estimated value exceeds the work from hydrolysis of six ATP molecules (one per FlaI subunit), $6 \times \Delta G_{\text{ATP}} \sim 5 \times 10^2$ pN·nm, given that ΔG_{ATP} is 8×10 pN·nm in cells¹³. If each FlaI subunit hydrolyzed a single ATP molecule per full archaeellar rotation, it follows that the archaeellar motor would have a paradoxical apparent efficiency of nearly 200%.

The simplest explanation for this apparent paradox is that FlaI uses more than six ATP molecules to power a single archaeellar rotation. The analogous F_1 -ATPase^{24–26} has three catalytic subunits cores, and three ATPs are hydrolyzed per turn of the rotor, which approaches $\sim 100\%$ efficiency¹³. Key to the mechanism is the strict cooperativity of three catalytic subunits, with the chemical state in one subunit returning to its original state after a full rotation of the rotor. This coincides with the asymmetric structure of the F_1 -ATPase shaft²⁷, as a particular side always faces just one of the three subunits in the specific chemical state (Fig. 4, left), confirmed through single-molecule observations using fluorescently labeled ATP (see Fig. 2e in ref. 24). Three ATP molecules are thus hydrolyzed per 360° rotation. In the archaeellar motor, we hypothesize that the cooperativity between subunits is similarly strict, but unlike the asymmetric F_1 -ATPase shaft, we propose that the structure against which FlaI rotates has n -fold symmetry (whether FlaI is part of the archaeellar stator or rotor) (Fig. 4, right). Parts of the n -fold

symmetric rotor will therefore always face n FlaI subunits in the corresponding specific state, resulting in n active subunits at any time. Therefore, a 360° rotor rotation would induce hydrolysis of $6 \times n$ ATPs by FlaI. To fulfill the archaeellar work requirement of 1000 pN·nm, n must be >1 . An n value of 2 is a good match for these requirements, with 12 ATP molecules hydrolyzed per full rotation, providing work of 1×10^3 pN·nm, and corresponding to an efficiency of 100%. Larger submultiples of six are also possible values of n ($n = 3$ and 6 would give efficiency of 67 and 33%, respectively), but a precedent for a value of 2 for n is set by structural studies: the archaeellar component FlaJ (ref. 1) may form a dimer, and the FlaI hexamer has two-fold symmetry instead of a pure six-fold symmetry⁸, as does its homolog PilB from the related type IV pilus²⁸, suggesting further significance of an as yet to be discovered two-fold element. Our torque measurement and energy estimation contribute critical information toward establishing how the archaeellar motor works.

Methods

Strains and cultivation. *H. salinarum* NRC1 (ATCC 700922) (ref. 29) was prepared as previously described³⁰ with modifications¹⁰. Cells were grown at 45 °C on agar plates (3.4 M NaCl, 0.12 M MgCl₂, 0.12 M MgSO₄, 0.08 M KCl, 0.5% (w/v) casamino acid, 0.002% (w/v) biotin, 0.005% (w/v) thiamine hydrochloride, 0.01% (w/v) L-tryptophan, 0.01% (w/v) uracil, 10 mM HEPES-NaOH (pH 7.0) and 1% (w/v) agar (Wako 010-08725)); and red-colored colonies were picked with the tip

of a micropipette and suspended in motility buffer (1.2 M NaCl, 0.7 M MgCl₂, 10 mM HEPES-NaOH (pH 7.0)).

Bead assay. All experiments were performed at room temperature, required for stability of the observation system for nanometer-resolution during recording. Streptavidin (Sigma-Aldrich) was conjugated with either carboxylated polystyrene beads (Polysciences) with sizes between 490 nm and 1.0 μm in diameter by a standard procedure using 1-ethyl-3-(3-dimethylaminopropyl)carbodiimide³¹ or

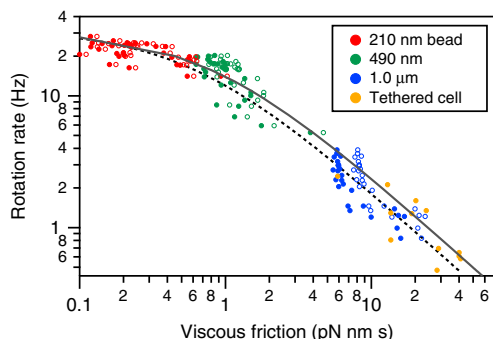


Fig. 3 Relationship between rotation rate and viscous friction of different markers. Viscous friction, γ , was estimated from the size, shape, and radius of rotation of markers (either beads or tethered cell) and the measured viscosity of the solution, $\eta = 1.35 \times 10^{-3}$ Pa·s. Sample sizes are 32, 31, 26 and 12 for red, green, blue and yellow dots, respectively. Filled and open circles show raw data and the same dataset after correction, taking into account the effect of interaction with the surface. Two lines show fitting with the rate assuming that the motor produces a constant torque, $f(\gamma) = T_a/2\pi(\gamma + \gamma_a)$, where f is the rotational rate; γ viscous friction; T_a the torque of the motor; and γ_a the constant. The dotted line is for raw data: $T_a = 1.2 \times 10^2$ pN·nm; $\gamma_a = 6.0 \times 10^{-1}$ pN·nm·s. The black line is for the dataset after correction: $T_a = 1.6 \times 10^2$ pN·nm; $\gamma_a = 8.1 \times 10^{-1}$ pN·nm·s. See the text for the interpretation of γ_a and its correction

amino-modified 210 nm beads (Polysciences) conjugated through biotin-(AC₅)₂-Sulfo-OSu, as previously described²⁵. The flow chamber was comprised of two coverslips (No. 1, 0.12–0.17-mm thickness; Matsunami Glass): 18 × 18 mm²; and 24 × 36 mm² glow-discharged with a hydrophilic treatment device (PIB-10; Vacuum Device). Two pieces of double-sided tape cut to approximately 5 mm wide and 30 mm in length serves as spacers for the two coverslips. The resulting flow chamber had an internal volume of ~7 μl (ref. 10). Biotinylated cells¹⁰ were mechanically sheared by passing 30 times in and out of a pipette tip and directly infused into the flow chamber in motility buffer. After incubation for 5 min, the chamber was rinsed with 20 μl motility buffer to remove unbound cells. Beads were subsequently infused and unbound beads washed off after incubation for 10 min. We did not estimate torque from data in which rotation exhibited periodic changes in speed (typically every 60°, Supplementary Fig. 1B).

Microscopy. An inverted microscope (Ti-E; Nikon Instruments) was equipped with a ×100 objective (Plan Fluor, N.A. 1.3; Nikon Instruments), a CMOS camera (DMK 23UX174; Imaging Source) set to the camera port in an eye-piece unit, a highly stable customized stage (Chukousha), and an optical table (RS-2000; Newport). The left camera port of the microscope was connected to a high-speed camera (HDR-20000; DigiMo) through a custom-made 3D tracking optical component, in which the wedge prism can be adjusted along the three axes in a blocked box. Images were recorded typically at 0.5-ms intervals with magnification to provide 98 × 98 nm² pixel size. Data were analyzed using Igor Pro (Wave Metrics) and ImageJ.

Calculation of drag coefficients of markers and archaeella. Solution viscosity was determined using a viscometer equipped with sensors driven by electromagnets to vibrate with a constant sine-wave vibration in reverse phase (SV-10; A&D Company). Viscosity measurements of buffer were taken ranging between 21.3 and 53.6 °C with calibration using distilled water. Viscosity was inversely proportional to temperature, and η of the solution was estimated to be 1.35×10^{-3} Pa·s under our measurement conditions. For beads, the equation $\gamma = 8\pi\eta r^3 + 6\pi\eta rR^2$ was applied where r is radius of bead and R the rotation radius^{14,32}. For corrections to estimate the precise torque in Fig. 3, we assumed the bead moved parallel to the glass surface and that the gap between the glass surface and the bead was equivalent to the width of the cell, 0.5 μm. Correction factors were thus calculated to be 1.4, 1.2, and 1.1 for 1.0-, 0.49-, and 0.21-μm beads, respectively (chapter 7–4 in ref. 18). For the tethered-cell assay, the drag coefficient of a rod, $\gamma = 1/3 \times \pi\eta L^3 \times [\ln(L/2r) - 0.66]^{-1}$, was applied where r is the radius of the rod cross-section and L is the length of the rod. In our measurements, the archaeellar pivot point is located at the end of the cell, and thus $1/2 \gamma$ with $L = 2 \times$ (cell length) was used. To discuss the contribution of viscous drag of a single

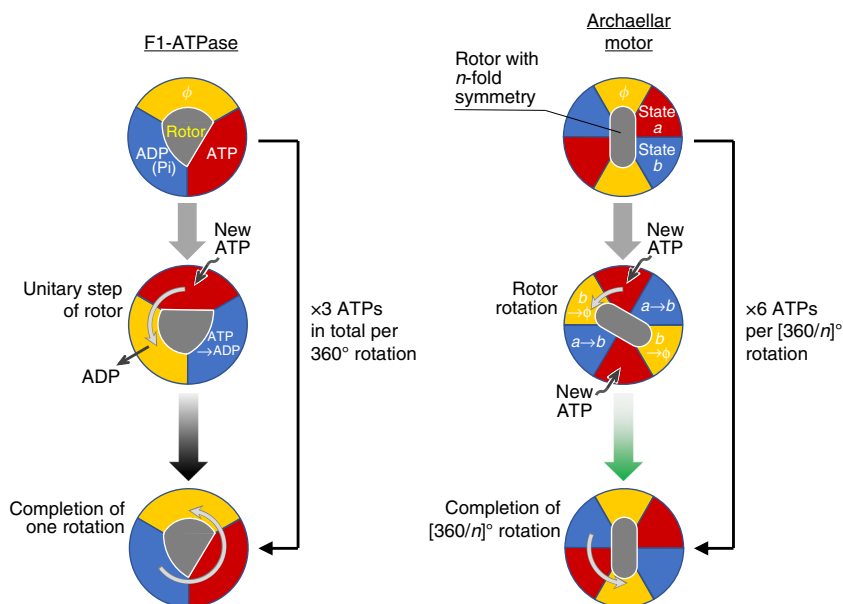


Fig. 4 A model for the mechanism of ATP hydrolysis by the archaeellar motor based on similarity to the F₁-ATPase. Left, The mechanism of the F₁-ATPase that we have previously demonstrated^{24–26, 33}. Two of the three catalytic subunits are occupied by nucleotides, either ATP (red) or ADP (blue), while the remaining subunit is empty (yellow). In this schematic, the positions of three subunits are fixed while the rotor rotates against them. Because the three catalytic subunits are cooperative, each subunit undergoes a determinate cycle through “empty state (ϕ)” → “ATP binding state” → “post-hydrolysis state” with each discrete 120° rotation. As a consequence, one F₁-ATPase with three catalytic subunits consumes three ATPs per rotation, with a single ATP hydrolysis per subunit per 360° rotation. Right, our model for the mechanism of ATP hydrolysis-driven archaeellar rotation. The principles are similar to the F₁-ATPase, except the catalytic cycle for each catalytic subunit repeats every $[360/n]^\circ$ rotation (green arrow) due to the n -fold symmetry of the rotor and six active sites. Note that the figure is conceptual: our model does not depend on a specific structure and is not intended to be structurally explicit. For simplicity, the schematic is illustrated with the assumption of $n = 2$, which is consistent with our results and observations of two-fold symmetry in the structure of the cyclic Flal hexamer⁸

archaellum, the equation, $\gamma = 2\pi\eta b^2 L(2p^2 + 4\pi^2 b^2) \times (p^2 + 4\pi^2 b^2)^{-1} \times [\ln(2p/r) - 0.5]^{-1}$ (ref. 17), was applied to estimate its frictional drag coefficient. γ was calculated to be 0.7 pN-nm-s with structural parameters¹⁰ $b = 0.22 \mu\text{m}$ (archaellum helix radius), $L = 4.3 \mu\text{m}$ (archaellum length), $p = 2.1 \mu\text{m}$ (archaellum helix pitch), and $r = 7 \text{ nm}$ (archaellum radius).

Reporting summary. Further information on research design is available in the Nature Research Reporting Summary linked to this article.

Data availability

The data that support the findings of this study are available from the corresponding author upon reasonable request.

Received: 30 September 2018 Accepted: 5 April 2019

Published online: 24 May 2019

References

- Albers, S. V. & Jarrell, K. F. The archaellum: how Archaea swim. *Front. Microbiol.* **6**, 23 (2015).
- Chaudhury, P., Tripp, P. & Albers, S. V. Expression, purification, and assembly of archaellum subcomplexes of *Sulfolobus acidocaldarius*. *Methods Mol. Biol.* **1764**, 307–314 (2018).
- Albers, S. V. & Jarrell, K. F. The archaellum: an update on the unique archaeal motility structure. *Trends Microbiol.* **26**, 351–362 (2018).
- Daum, B. et al. Structure and in situ organisation of the *Pyrococcus furiosus* archaellum machinery. *Elife* **6**, e27470 (2017).
- Jarrell, K. F. & Albers, S. V. The archaellum: an old motility structure with a new name. *Trends Microbiol.* **20**, 307–312 (2012).
- Streif, S., Staudinger, W. F., Marwan, W. & Oesterhelt, D. Flagellar rotation in the archaeon *Halobacterium salinarum* depends on ATP. *J. Mol. Biol.* **384**, 1–8 (2008).
- Ghosh, A., Hartung, S., van der Does, C., Tainer, J. A. & Albers, S. V. Archaeal flagellar ATPase motor shows ATP-dependent hexameric assembly and activity stimulation by specific lipid binding. *Biochem. J.* **437**, 43–52 (2011).
- Reindl, S. et al. Insights into FlaI functions in archaeal motor assembly and motility from structures, conformations, and genetics. *Mol. Cell* **49**, 1069–1082 (2013).
- Chaudhury, P. et al. The nucleotide-dependent interaction of FlaH and FlaI is essential for assembly and function of the archaellum motor. *Mol. Microbiol.* **99**, 674–685 (2015).
- Kinosita, Y., Uchida, N., Nakane, D. & Nishizaka, T. Direct observation of rotation and steps of the archaellum in the swimming halophilic archaeon *Halobacterium salinarum*. *Nat. Microbiol.* **1**, 16148 (2016).
- Yajima, J., Mizutani, K. & Nishizaka, T. A torque component present in mitotic kinesin Eg5 revealed by three-dimensional tracking. *Nat. Struct. Mol. Biol.* **15**, 1119–1121 (2008).
- Deschout, H. et al. Precisely and accurately localizing single emitters in fluorescence microscopy. *Nat. Methods* **11**, 253–266 (2014).
- Yasuda, R., Noji, H., Kinosita, K. Jr. & Yoshida, M. F₁-ATPase is a highly efficient molecular motor that rotates with discrete 120° steps. *Cell* **93**, 1117–1124 (1998).
- Yasuda, R., Noji, H., Yoshida, M., Kinosita, K. Jr. & Itoh, H. Resolution of distinct rotational substeps by submillisecond kinetic analysis of F₁-ATPase. *Nature* **410**, 898–904 (2001).
- Chen, X. & Berg, H. C. Torque-speed relationship of the flagellar rotary motor of *Escherichia coli*. *Biophys. J.* **78**, 1036–1041 (2000).
- Li, G. & Tang, J. X. Low flagellar motor torque and high swimming efficiency of *Caulobacter crescentus* swarmer cells. *Biophys. J.* **91**, 2726–2734 (2006).
- Sowa, Y., Hotta, H., Homma, M. & Ishijima, A. Torque-speed relationship of the Na⁺-driven flagellar motor of *Vibrio alginolyticus*. *J. Mol. Biol.* **327**, 1043–1051 (2003).
- Happel, J. & Brenner, H. *Low Reynolds Number Hydrodynamics: With Special Applications to Particulate Media* (Martinus Nijhoff Publishers, The Hague, 1983).
- Kinosita, Y. et al. Unitary step of gliding machinery in *Mycoplasma mobile*. *Proc. Natl Acad. Sci. USA* **111**, 8601–8606 (2014).
- Uenoyama, A. & Miyata, M. Gliding ghosts of *Mycoplasma mobile*. *Proc. Natl Acad. Sci. USA* **102**, 12754–12758 (2005).
- Pate, E., Wilson, G. J., Bhimani, M. & Cooke, R. Temperature dependence of the inhibitory effects of orthovanadate on shortening velocity in fast skeletal muscle. *Biophys. J.* **66**, 1554–1562 (1994).
- Kojima, H., Muto, E., Higuchi, H. & Yanagida, T. Mechanics of single kinesin molecules measured by optical trapping nanometry. *Biophys. J.* **73**, 2012–2022 (1997).
- Crevel, I., Carter, N., Schliwa, M. & Cross, R. Coupled chemical and mechanical reaction steps in a processive *Neurospora* kinesin. *EMBO J.* **18**, 5863–5872 (1999).
- Nishizaka, T. et al. Chemomechanical coupling in F₁-ATPase revealed by simultaneous observation of nucleotide kinetics and rotation. *Nat. Struct. Mol. Biol.* **11**, 142–148 (2004).
- Masaike, T., Koyama-Horibe, F., Oiwa, K., Yoshida, M. & Nishizaka, T. Cooperative three-step motions in catalytic subunits of F₁-ATPase correlate with 80 degrees and 40 degrees substep rotations. *Nat. Struct. Mol. Biol.* **15**, 1326–1333 (2008).
- Sugawa, M. et al. F₁-ATPase conformational cycle from simultaneous single-molecule FRET and rotation measurements. *Proc. Natl Acad. Sci. USA* **113**, E2916–E2924 (2016).
- Abrahams, J. P., Leslie, A. G., Lutter, R. & Walker, J. E. Structure at 2.8 Å resolution of F₁-ATPase from bovine heart mitochondria. *Nature* **370**, 621–628 (1994).
- McCallum, M., Tammam, S., Khan, A., Burrows, L. L. & Howell, P. L. The molecular mechanism of the type IVa pilus motors. *Nat. Commun.* **8**, 15091 (2017).
- Ng, W. V. et al. Genome sequence of *Halobacterium* species NRC-1. *Proc. Natl Acad. Sci. USA* **97**, 12176–12181 (2000).
- Tripepi, M., Imam, S. & Pohlschroder, M. Haloferax volcanii flagella are required for motility but are not involved in PibD-dependent surface adhesion. *J. Bacteriol.* **192**, 3093–3102 (2010).
- Nishizaka, T., Miyata, H., Yoshikawa, H., Ishiwata, S. & Kinosita, K. Jr. Unbinding force of a single motor molecule of muscle measured using optical tweezers. *Nature* **377**, 251–254 (1995).
- Howard, J. *Mechanics of Motor Proteins and the Cytoskeleton* (Sinauer Associates, Inc., Sunderland, MA, 2001).
- Adachi, K. et al. Coupling of rotation and catalysis in F₁-ATPase revealed by single-molecule imaging and manipulation. *Cell* **130**, 309–321 (2007).

Acknowledgements

The authors thank M. Beeby, Y. Sowa and R. Kamiya for discussions that were critical to preparation of the manuscript and T. A. Katoh for microscopy assistance and figure preparation. This study was supported in part by a Grant-in-Aid for Scientific Research on Innovative Areas [“Fluctuation & Structure” of JP16H00792 (to N.U.), JP16H00808 (to T.N.) and JP26103527 (to T.N.), “Cilia & Centrosomes” of JP87003306 (to T.N.), and “Motility Machinery” of JP15H01329 (to D.N.)] and by Japan Society for the Promotion of Science KAKENHI [Grants JP16H06230 (to D.N.) and JP15H04364 (to T.N.)]. Y.K. was the recipient of JSPS Fellowship for Japan Junior Scientists (15J12274).

Author contributions

S.I., Y.K. and T.N. designed research; Y.K. performed the early research; S.I. performed research; T.N. constructed the microscope and analysis software; N.U., D.N. and T.N. wrote the paper.

Additional information

Supplementary information accompanies this paper at <https://doi.org/10.1038/s42003-019-0422-6>.

Competing interests: The authors declare no competing interests.

Reprints and permission information is available online at <http://npg.nature.com/reprintsandpermissions/>

Publisher’s note: Springer Nature remains neutral with regard to jurisdictional claims in published maps and institutional affiliations.



Open Access This article is licensed under a Creative Commons Attribution 4.0 International License, which permits use, sharing, adaptation, distribution and reproduction in any medium or format, as long as you give appropriate credit to the original author(s) and the source, provide a link to the Creative Commons license, and indicate if changes were made. The images or other third party material in this article are included in the article’s Creative Commons license, unless indicated otherwise in a credit line to the material. If material is not included in the article’s Creative Commons license and your intended use is not permitted by statutory regulation or exceeds the permitted use, you will need to obtain permission directly from the copyright holder. To view a copy of this license, visit <http://creativecommons.org/licenses/by/4.0/>.

© The Author(s) 2019